

An integrated microwave-to-optics interface for scalable quantum computing

Received: 8 October 2022

Accepted: 31 August 2023

Published online: 5 October 2023



Matthew J. Weaver^{1,2}, Pim Duivesteyn^{1,2}, Alexandra C. Bernasconi^{1,2}, Selim Scharmer^{1,2}, Mathilde Lemang¹, Thierry C. van Thiel¹, Frederick Hijazi¹, Bas Hensen¹, Simon Gröblacher¹✉ & Robert Stockill¹✉

Microwave-to-optics transduction is emerging as a vital technology for scaling quantum computers and quantum networks. To establish useful entanglement links between qubit processing units, several key conditions must be simultaneously met: the transducer must add less than a single quantum of input-referred noise and operate with high efficiency, as well as large bandwidth and high repetition rate. Here we present a design for an integrated transducer based on a planar superconducting resonator coupled to a silicon photonic cavity through a mechanical oscillator made of lithium niobate on silicon. We experimentally demonstrate its performance with a transduction efficiency of 0.9% with 1 μ W of continuous optical power and a spectral bandwidth of 14.8 MHz. With short optical pulses, we measure the added noise that is limited to a few photons, with a repetition rate of up to 100 kHz. Our device directly couples to a 50 Ω transmission line and can be scaled to a large number of transducers on a single chip, laying the foundations for distributed quantum computing.

Quantum processors and quantum networks have the potential to revolutionize information technology. They substantially expand on the existing capabilities of modern computers by solving previously intractable problems and enhance the security of information sharing over networks^{1–3}. To achieve superior performance compared with classical computers on practical computational tasks, state-of-the-art quantum computers will need to increase the number of high-quality qubits by multiple orders of magnitude³. Several different realizations of such large-scale quantum processors are currently being pursued^{4,5}, all with their own advantages and challenges. Some of the most advanced and promising quantum computers to date are based on superconducting qubits operating at cryogenic temperatures, which are currently capable of forming processors with up to 433 qubits on a single chip⁶. However, engineering difficulties such as the limited cooling power of cryogenic systems and space constraints of the microwave drive and readout lines pose severe restrictions on the scalability of these quantum computers.

Quantum interconnects can enable individual quantum modules to be incorporated into a multiprocessor architecture, surpassing the

limits of single cryogenic systems and chip-scale fabrication^{7–9}. At the same time, many leading stationary qubit implementations exchange information with microwave-frequency photons, limiting the reach of such connections to short distances in a cryogenic environment¹⁰. Accordingly, transduction between microwave and optical frequencies is a key technology, enabling long-range channels at room temperature. Several different technologies are being explored for this task, including direct transduction^{11–13} and transduction assisted by an intermediary system such as a resonant mechanical mode^{14–17}, lower-frequency mechanical mode^{18,19}, atomic state^{20–22} or magnon mode²³. Despite these advances, a scalable quantum transducer that can interface with multiple qubits with high efficiency, large bandwidth and low added noise remains an outstanding challenge^{24,25}.

The properties of the systems that would benefit from quantum transduction to optical wavelengths set the specific requirements for the transducer. Integrated two-dimensional qubit systems have reached coherence times exceeding tens of microseconds^{26,27}. To avoid a bottleneck, an ideal transducer should, therefore, operate with a repetition rate and bandwidth much greater than the inverse lifetime

¹QphoX B.V., Delft, The Netherlands. ²These authors contributed equally: Matthew J. Weaver, Pim Duivesteyn, Alexandra C. Bernasconi, Selim Scharmer.

✉ e-mail: simon@qphox.eu; rob@qphox.eu

of the qubits ($\gg 10$ kHz). Distributed quantum computation will probably require many transducers in parallel to allow for fully remote gates between error-corrected qubits^{28,29}, which necessitates an integrated system with many transducers on a single chip. Furthermore, most microwave-frequency quantum systems can couple to transmission lines, which makes external coupling via $50\ \Omega$ lines an attractive and flexible approach^{26,30}. Finally, the transducer must not adversely affect the performance of the quantum computation, requiring high efficiency and added noise below a single photon to generate remote entanglement between multiple processors³¹. Although devices based on three-dimensional cavity geometries have demonstrated efficiencies up to 47% with noise levels close to the quantum regime in one instance³² as well as low added noise N_{add} of 0.16 in another¹³, the former operated over a bandwidth of ≤ 200 Hz and the latter required operating at a repetition rate of ≤ 10 Hz. As such, these approaches are challenging to scale to large transducer numbers. Another chip-scale approach recently demonstrated transduction with $N_{\text{add}} \approx 0.5$ directly coupled to a superconducting qubit¹⁶, but quasiparticle generation from optical absorption destroyed the qubit state and limited the transducer repetition rate. So far, no transducer operating in the quantum regime has demonstrated the bandwidth, repetition rate and scalability required for networking quantum processors.

Here we report on the experimental realization of efficient, large-bandwidth and low-noise transduction between microwave and optical frequencies by using a mechanical resonator as an intermediary. Our system is based on a thin-film lithium niobate on a silicon-on-insulator platform³³, allowing us to simultaneously realize a strongly coupled electromechanical and a high-performance optomechanical interface. The device is extremely compact ($0.15\ \text{mm}^2$; Fig. 1f) and scalable, converting between a $50\ \Omega$ impedance line and an optical fibre with a 14.8 MHz spectral bandwidth, at repetition rates up to 100 kHz. We operate the transducer close to the quantum regime with only 6.2 ± 1.8 photons of added noise. Our chip design already features multiple transducers on a single chip, and modest improvements will allow for the generation of entanglement between remote quantum modules in parallel.

Transducer description

The central part of the transducer device consists of a suspended silicon nanobeam with a short phononic waveguide that is terminated by a piezoelectric block of lithium niobate. The phononic and photonic crystal of the nanobeam form a defect mode for optical excitations at around $\lambda_0 \approx 1,550$ nm and mechanical excitations at around $\omega_m/2\pi \approx 5$ GHz (ref. 34). These modes are coupled to one another predominantly through the photoelastic effect. Owing to this interaction, the application of an optical pump tone red-detuned from optical resonance by the mechanical frequency realizes a state swap between phonons occupying the mechanical mode and optical photons on resonance³⁵.

Interaction between the mechanical mode and microwave-frequency photons is realized through resonant piezoelectric coupling. To achieve this, we include a small piece of lithium niobate at the end of the nanobeam, electrically contacted on each side (Fig. 1e,i). The holes of the nanobeam are shaped such that the mechanical mode leaks out of the defect and couples to the lithium niobate block, with the result that the different portions of the beam hybridize into a single extended mechanical mode.

To efficiently couple microwave photons between the $50\ \Omega$ transmission line and the high-impedance piezoelectric device, we include a half-wavelength microwave resonator, terminated by the lithium niobate block (Fig. 1b,f). The resonator is formed from a 160-nm-wide superconducting molybdenum–rhenium (MoRe) nanowire. We pattern the resonator into a ladder geometry, which allows for tuning of the resonator frequency by up to 10% by applying a magnetic flux resulting from a nearby superconducting coil³⁶. This tuning range ensures that we can match the microwave resonator to the mechanical

mode frequency of the device. We simulate the resulting electrical, mechanical and optical modes of the full device and sweep the length and width of the lithium niobate block to ensure mechanical hybridization between the block and optomechanical defect. These simulations predict simultaneous single-photon optomechanical coupling strengths of $g_{\text{om},0}/2\pi = 530$ kHz and piezoelectric coupling rates of up to $g_{\text{em}}/2\pi = 18$ MHz (Supplementary Section I).

Our devices are fabricated from a 320-nm-thick layer of X-cut lithium niobate bonded to a high-resistivity silicon-on-insulator wafer. We orient the long axis of the device at an angle of 30° from the Z axis of the lithium niobate to maximize the electromechanical coupling rate³⁷, which induces some torsional asymmetry in the breathing mode. We first pattern and remove the lithium niobate layer through ion-beam milling, leaving the small block shown in Fig. 1i. We then pattern and etch the silicon layer to form the nanobeam (Fig. 1h). Finally, we deposit the MoRe film for the resonator and suspend the device by selectively etching the oxide layer. We use etch holes around the microwave resonator to remove the oxide layer from underneath, increasing the microwave quality factor of the device.

Continuous-wave transduction

The device is cooled down to around 25 mK inside a dilution refrigerator. A laser field is coupled through a lensed optical fibre into a tapered reflective waveguide, which is evanescently coupled to the optical resonator, allowing us to measure the optical mode in reflection through a circulator³⁸. As the first step, we characterize the device parameters. Figure 1l shows the overcoupled optical resonance we measure when scanning the input laser frequency and recording the reflected optical power. We find the device's resonance at $\lambda_0 = 1,552.6$ nm, with an external coupling rate $\kappa_{\text{oe}}/2\pi = 3.65 \pm 0.14$ GHz and intrinsic loss rate $\kappa_{\text{oi}}/2\pi = 1.34 \pm 0.07$ GHz. We characterize the mechanical spectrum of the device by stabilizing the laser frequency red-detuned by ω_m with respect to the optical resonance and measuring the reflected signal through heterodyne detection. The resulting thermal spectrum of the mechanics is displayed in Fig. 1k, showing a mode centred at $\omega_m/2\pi = 5.043$ GHz with a linewidth of $\kappa_m/2\pi = 2.63 \pm 0.12$ MHz. The microwave resonator on the chip is capacitively coupled to a $50\ \Omega$ transmission line. The microwave mode is measured in transmission and is displayed in Fig. 1j, with a resonance centred at 5.07 GHz, an intrinsic loss rate of $\kappa_{\text{ei}}/2\pi = 1.23 \pm 0.11$ MHz and an external coupling rate of $\kappa_{\text{ee}}/2\pi = 2.21 \pm 0.10$ MHz. This measurement was taken with a magnetic field of approximately 3 mT (Supplementary Table 1 provides a full list of parameters).

We now proceed to characterize the interaction between the mechanical and microwave sub-components. The electromechanical coupling is measured by applying a continuous microwave drive tone and tuning the microwave resonator's frequency by applying a magnetic field (Fig. 2a). As the resonator frequency approaches the optically active mechanical mode at 5.043 GHz, we observe the characteristic avoided crossing of the resonance frequency, as the mechanical and electrical modes become hybridized. From the size of this avoided crossing, we can directly extract the coupling rate between the mechanical mode and microwave mode, which is $g_{\text{em}}/2\pi = 7.4 \pm 0.9$ MHz, larger than both κ_e and κ_m . Sources of discrepancy between the simulated and experimentally measured values include the amount of parasitic capacitance in the microwave resonator, as well as the exact thickness of MoRe deposited on the sides of the lithium niobate block. This strong electromechanical coupling is evidence of the high-cooperativity interface required for efficient and noise-free transduction. Given the mechanical and electrical damping rates, we extract a cooperativity of $C_{\text{em}} = 4g_{\text{em}}^2/\kappa_e\kappa_m = 24.2 \pm 4.4$.

To demonstrate the microwave-to-optics transduction capabilities of the device (upconversion), we input a frequency-swept microwave tone, which we convert with a continuous optical pump red-detuned from the optical resonance. We measure the

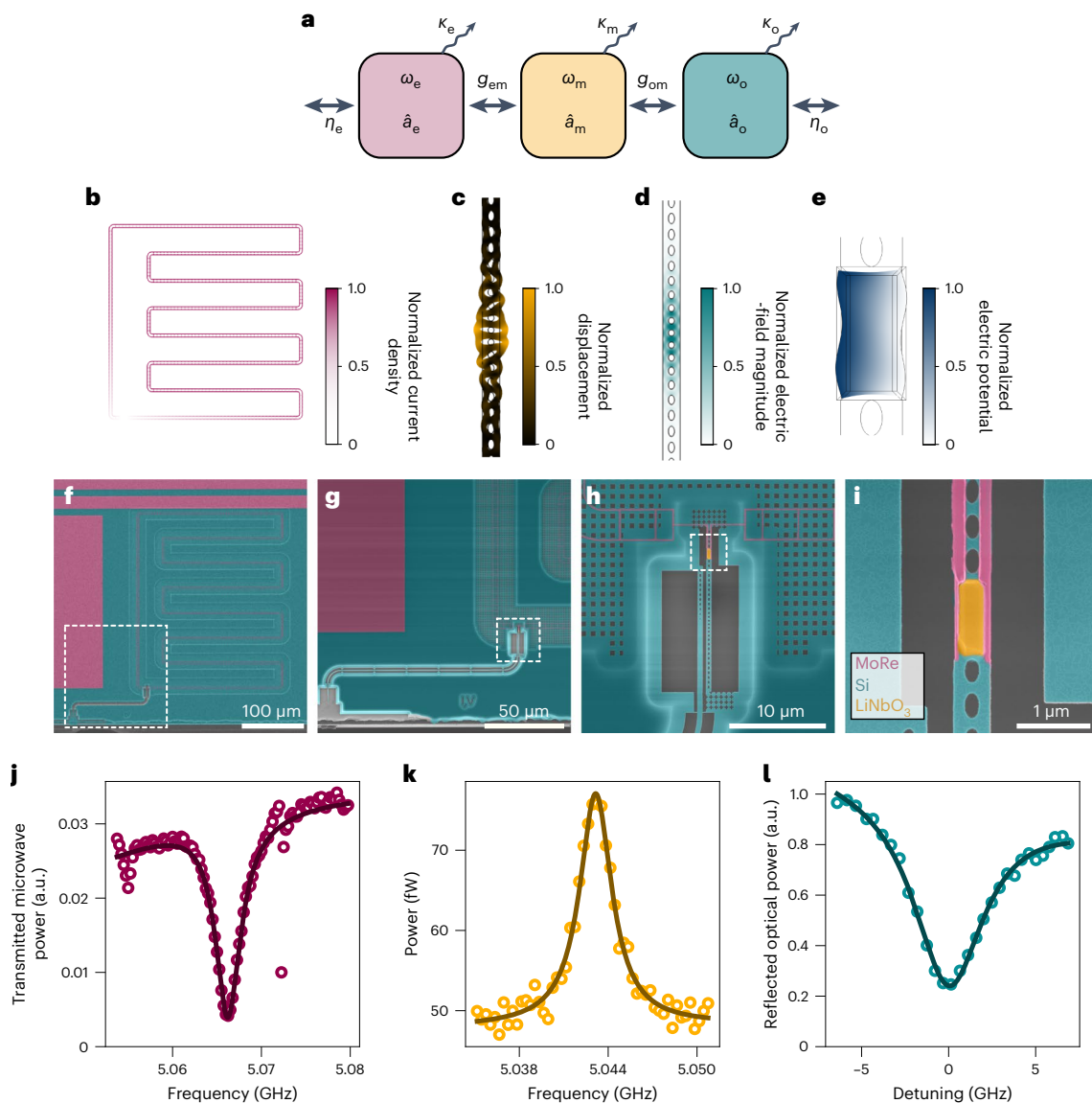


Fig. 1 | Microwave-to-optical transduction device. **a**, Optomechanical transducer consisting of three coupled bosonic modes: microwave (magenta), mechanical (yellow) and optical (cyan). Each has a frequency of $\omega/2\pi$, bosonic operator \hat{a} and loss rate $\kappa/2\pi$. The electrical and optical modes couple to additional external channels with efficiency η , as well as to the mechanical mode with coupling rate g_{em} and g_{om} . **b–e**, Finite element analysis of the current density of the microwave resonator (**b**), displacement of the mechanical mode (**c**), total electric field magnitude of the optical mode (**d**) and electrical potential of the piezoelectric resonator (**e**). All the mode distributions have been normalized to their maximum value. **f–i**, Scanning electron micrographs of a representative transducer from the same fabrication run. A superconducting MoRe nanowire loop microwave resonator (magenta) is capacitively coupled to an external

transmission line (**f**). An optical waveguide separates the optical-fibre output (bottom left) from the superconducting resonator (top right, **g**). The transduction region is fabricated into a silicon layer (cyan) and consists of a co-localized photonic and phononic crystal cavity linked by a phononic waveguide to a lithium niobate (LiNbO₃) piezoelectric block (yellow). The optical cavity is evanescently coupled to the optical waveguide (**h**). At the end of the phononic waveguide, electrodes from the microwave resonator (magenta) contact the piezoelectric block (**i**). **j**, Transmitted microwave power through the transmission line reveals the microwave resonance dip at 5.07 GHz. **k**, Thermal motion of the mechanical resonance measured in the modulation of the optical signal reflected from the device. **l**, Optical resonance of the photonic crystal cavity measured using the reflected laser light from the transducer.

upconverted signal by detecting the resulting optical sideband in the reflected light from the device through heterodyne detection. To measure transduction from optics to microwave (downconversion), we supply a signal on resonance with the optical cavity by modulating the red-detuned pump using an electro-optic modulator, and directly measure the output microwave tone from the device. The upconversion and downconversion scattering parameters (including all the microwave and optical loss and gain in the setup) as a function of the microwave drive and the detuning of the microwave resonator are displayed in Fig. 2b,c, respectively. The transduction is at its maximum when the microwave resonator approaches the mechanical

frequency, and the two traces display the same avoided crossing as in microwave spectroscopy.

We further supplement our continuous transduction measurements with measurements of off-resonant reflected microwave and optical signals, which allow us to calibrate the loss and gain in the microwave and optical lines, and extract the bidirectional transduction efficiency of the transducer (Supplementary Section III). We define transduction efficiency here as the waveguide-to-waveguide efficiency, excluding the fibre coupling efficiency. The resulting two-dimensional map of efficiency is plotted in Fig. 2d. We find that for a supplied optical pump power of 1 μ W, the peak efficiency we extract is around 0.9% with

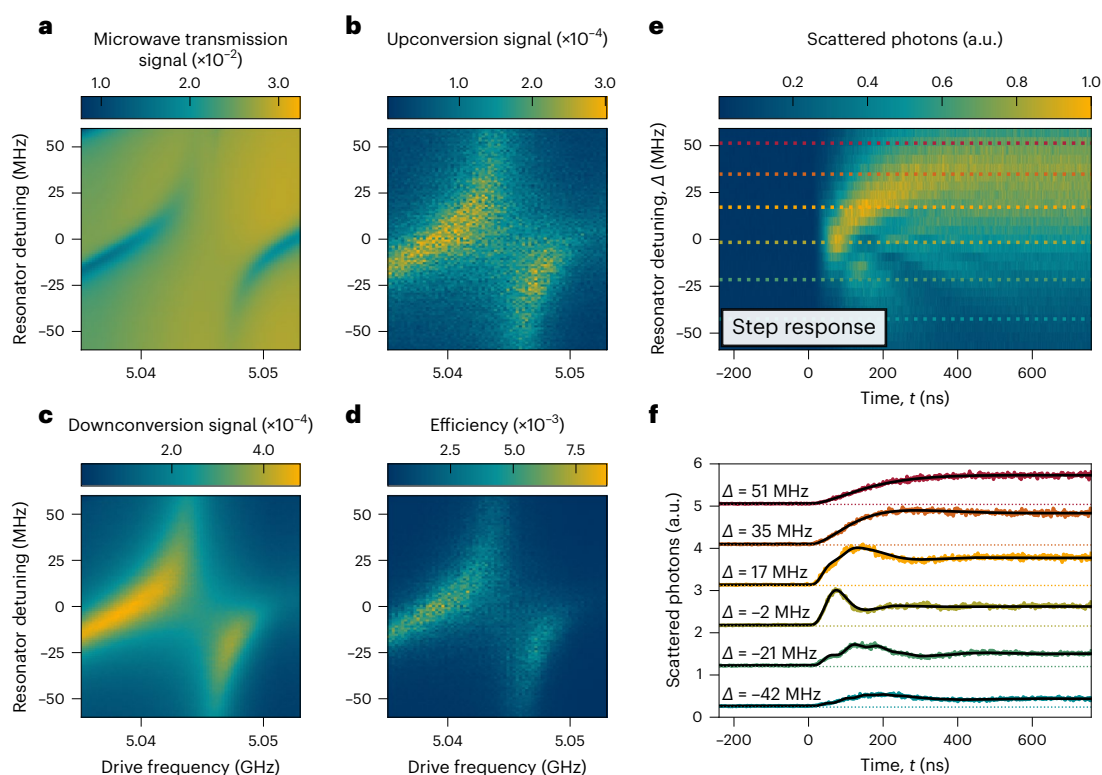


Fig. 2 | Resonant electromechanical coupling and bidirectional transduction.

a, The frequency of the microwave resonator is tuned into resonance with the mechanical mode using a magnetic field to observe electromechanical coupling and transduction. We measure the microwave field going through the transmission line coupled to the microwave resonator. The avoided crossing at the frequency of the mechanical mode displays a strong coupling between the mechanical and electrical modes, with $g_{\text{em}}/2\pi = 7.4 \pm 0.9$ MHz. **b**, Upconversion of the microwave signal to the optical domain detected using optical heterodyne

measurement. **c**, Downconversion of an optical signal to the microwave domain collected via the microwave transmission line. As expected, both upconversion and downconversion follow the features of the hybridized electromechanical mode. **d**, Continuous-drive transduction efficiency of the device extracted using a four-port measurement, revealing a maximum efficiency of 0.9%. **e**, Step response of mechanical resonance to a microwave drive, which turns on at time $t = 0$. **f**, Individual cross-sections fit by a model that yields mean values of $g_{\text{em}}/2\pi = 8.7 \pm 0.6$ MHz and $\kappa_e = 4.9 \pm 0.5$ MHz.

a spectral bandwidth of $2g_{\text{em}}/2\pi = 14.8 \pm 1.8$ MHz. For optical powers much greater than this, the efficiency is limited by nonlinear effects such as thermal bistability of the optical cavity and reduction in the microwave resonator's quality factor due to residual absorption of the laser.

Pulsed transduction

Pulsing the optical and microwave inputs allows us to access the time-domain response of the device. We first look at the electromechanically enhanced excitation of the mechanical mode. To do this, we send in a continuous low-power optical drive and a fixed-frequency 2- μ s-long microwave pulse on resonance with the mechanical mode. We filter the upconverted signal from the reflected red-detuned pump light with narrow-linewidth Fabry–Pérot resonators³⁸. The filtered light is detected using a superconducting-nanowire single-photon detector. We correlate the arrival time of photons following the start of the microwave pulse (at time $t = 0$). By sweeping the detuning of the microwave resonator with respect to the microwave tone Δ and measuring the scattered photons from the device (Fig. 2e,f), we can directly extract the time dynamics of transduction. As expected for a high-cooperativity interface, as the microwave resonator becomes resonant with the mechanical mode, the rise time of electromechanical loading decreases and coherent oscillations between the resonator mode and mechanical mode appear. We fit the time response to the microwave drive step with a simple model (Supplementary Section VII) to extract the electromechanical cooperativity of our device, which we find to be $C_{\text{em}} = 33 \pm 10$, in good agreement with the expected value for our independently measured parameters.

Now that we have characterized the time dynamics of the electromechanical interface, we move to also use short optical pulses. We start by measuring the thermal occupation of the mechanical mode as a function of pulse energy using a sideband asymmetry measurement³⁸. We use 40-ns-long optical pump pulses, filtering out the reflected optical pump and sending the scattered photons at the cavity frequency to the superconducting-nanowire single-photon detector (total detection efficiency $\eta_{\text{det}} = 0.048$). Figure 3a shows the resulting detection probabilities and a clear asymmetry between the blue- and red-detuned pulses. The extracted thermal occupation (n_{th}) is shown in Fig. 3b. For low pulse energies, $n_{\text{th}} < 1$, indicating that the mechanical mode is in the quantum ground state with a high probability. As microwaves are first loaded into the mechanical resonator with an efficiency η_{em} before thermal noise is added, the added noise referred to the input is $N_{\text{add}} = n_{\text{th}}/\eta_{\text{em}}$ photons. For the subsequent pulsed transduction measurements, we operate in the regime where the added thermal noise to the transduction process is limited to $N_{\text{add}} \approx (0.41 \pm 0.05)/\eta_{\text{em}}$ photons.

For a full pulsed transduction characterization of our device, we now input 60-ns-long microwave pulses fixed at the mechanical frequency into the transducer, followed by a 40 ns red-detuned optical pulse at a repetition rate of 100 kHz. The converted optical-output photons from the transducer are filtered and detected using the superconducting-nanowire single-photon detector. Figure 3c shows the photon detection probability as a function of input microwave photon number. The input microwave photon number is calibrated based on line attenuation measurements (Supplementary Section IV). The detected optical photons are the sum of the converted microwave

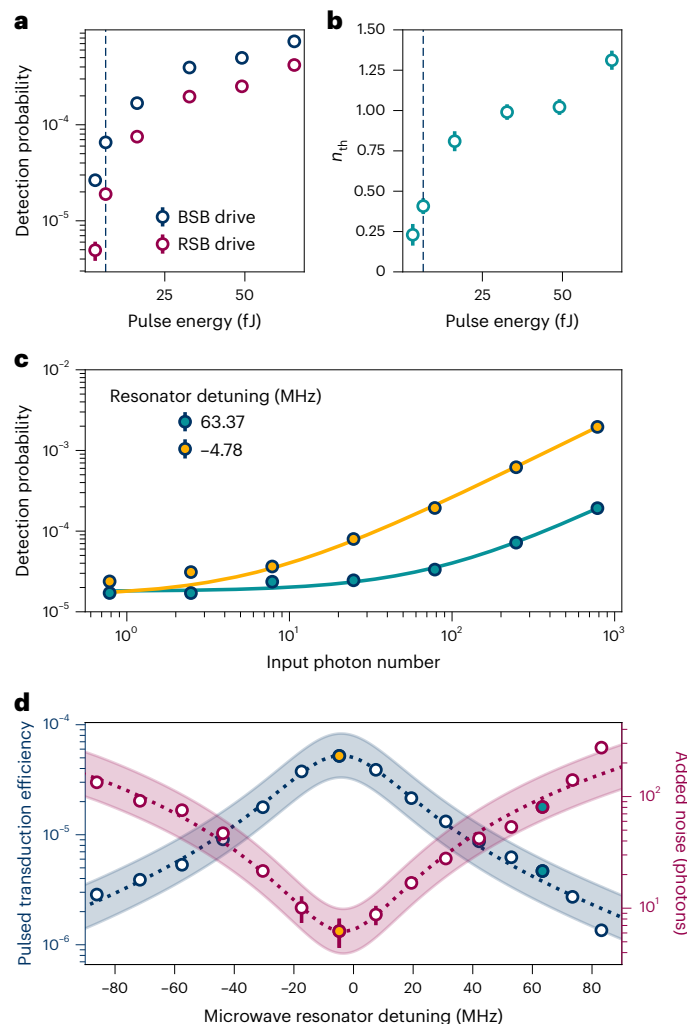


Fig. 3 | Pulsed transduction and added noise. **a**, Detection probabilities for photons generated with an optical pump red-detuned by ω_m (RSB) and blue-detuned by ω_m (BSB) from cavity resonance, while the microwave drive is turned off. **b**, Asymmetry between these two scattering rates can be used to extract the thermal occupation of the mechanical mode n_{th} as a function of optical pulse energy. The dashed line indicates the optical pulse power used for the pulsed transduction measurements, a power for which the mechanical mode is predominantly in the ground state. **c**, Detection probability of an upconverted optical photon as a function of input microwave photons for two different microwave resonator detunings. The independent linear fits allow us to extract the transduction efficiency (blue) and added noise (magenta). **d**, Waveguide-to-waveguide transduction efficiency (blue) and added noise (magenta) as a function of microwave resonator detuning. The shaded regions indicate uncertainties arising from the microwave input attenuation. The yellow and green points correspond to the power sweeps in **c**. In **a–d**, the centre of each point is the mean value and the error bars represent one standard deviation above and below the mean.

photons ($\eta_{det}\eta_{om}\eta_{em}n_{mic}$) and the optomechanically converted noise photons ($\eta_{det}\eta_{om}n_{th}$), where n_{mic} is the initial number of microwave photons, η_{det} is the overall detection efficiency, η_{om} is the optomechanical and η_{em} is the electromechanical transduction efficiency. We then sweep the detuning of the microwave resonator with respect to the mechanical frequency and record the pulsed transduction efficiency and added noise N_{add} (Fig. 3d). From this measurement, we find a peak transduction efficiency of $(5.21 \pm 0.03) \times 10^{-5}$ and minimum added noise of $N_{add} = 6.2 \pm 1.8$ photons.

We can use our model from the transduction time dynamics (Fig. 2f) to determine the electromechanical loading efficiency.

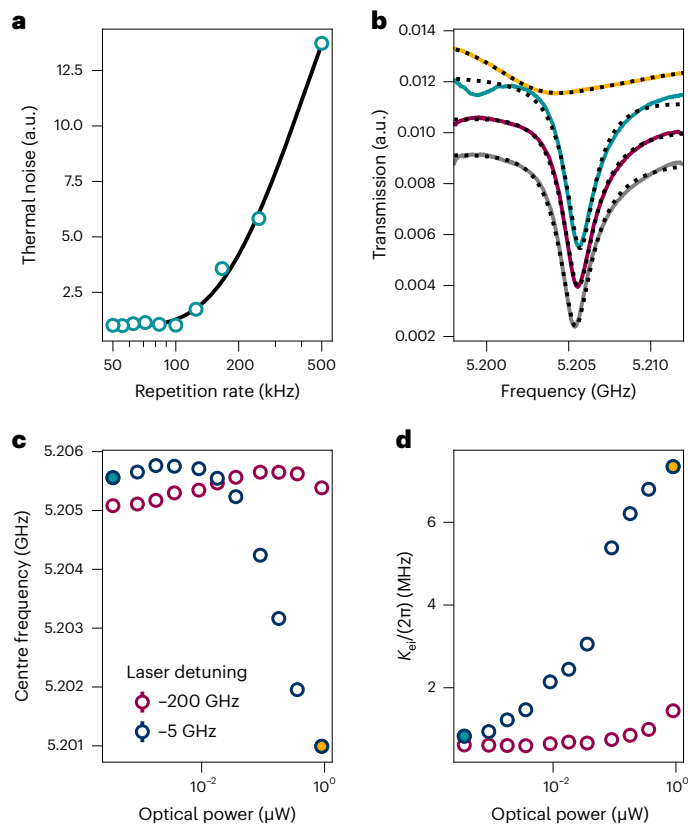


Fig. 4 | Repetition rate and quasiparticle generation. **a**, Detected noise photons (normalized to 50 kHz repetition rate) which increase with the repetition rate. An exponential fit (solid line) yields the thermal recovery time. **b**, Microwave transmission through the resonator measured under four conditions: laser excitation off (grey), pulsed excitation with 5 fJ pulses at 100 kHz repetition rate (magenta) and continuous excitation with 1 μ W (yellow) and 400 pW, the same average power as for the pulsed case (cyan). **c, d**, Microwave resonator frequency (c) and internal loss rate κ_{ei} (d) depend on the optical power sent to the transducer and the laser detuning from the optical resonance. The cyan-filled (yellow-filled) points mark the powers and detunings used for the cyan (yellow) traces shown in **b**.

From this model, we find an efficiency of $\eta_{em} \approx 0.12$, which is substantially higher than the value of $\eta_{em} = 0.053 \pm 0.008$ extracted from the measurements shown in Fig. 3d. From the microwave transmission data (Supplementary Figs. 2 and 6 and Supplementary Section IX), we observe multiple strongly coupled modes that are relatively close in frequency to the mode of interest. By extending the model to include one extra neighbouring mode, we see that the expected electromechanical loading efficiency drops to approximately 0.06 (Supplementary Section VII). With this reduced loading efficiency, the expected value for N_{add} from the sideband asymmetry measurement is 6.8 ± 0.8 photons, in good agreement with the calibrated value above.

As a final step, we investigate the limits of our transduction rate. To do this, we input a red-detuned laser into the cavity and determine the thermal occupation of the mechanical mode by measuring optomechanically scattered noise photons, without a microwave drive. We perform this measurement for an increasing repetition rate (Fig. 4a). The relative thermal noise remains constant up to a repetition rate of approximately 100 kHz, above which residual phonons from the previous excitation pulse increase the scattering rate. We find a thermal recovery time of 2 μ s, which is around the same order of magnitude as the mechanical mode lifetimes in the system.

We further measure the impact of optical light in the transducer on the frequency and quality factor of the superconducting resonator. Strong optical fields can pose a major challenge for integrated transducers as optical photons can generate quasiparticles (directly or via

thermal heating), which degrade or even destroy the superconducting state¹⁶. To determine the impact of quasiparticle generation on our transducer, we measure the microwave resonance frequency shift and internal loss rate as a function of optical power (Fig. 4c,d). Individual traces without light and with the optical powers and wavelengths used in the continuous (1 μ W continuous wave) and pulsed measurements (5 f) pulses, 0.5 nW average power) are displayed in Fig. 4b. We see a frequency shift of -3.74 ± 0.07 MHz and a 9.6 ± 1.0 times greater internal loss rate in the continuous case, but in the pulsed case, we find a frequency shift of only $+200 \pm 80$ kHz and a negligible loss rate change. We also repeat the optical power sweep at 200 GHz detuned from the optical resonance and observe a drastically decreased response to optical power. We, therefore, conclude that the resonator changes are a result of the optical field inside the cavity, and that losses of the fibre-to-waveguide coupling play a negligible role. Overall, although we can observe some effects of quasiparticle generation, they are not strong enough to limit the low-noise pulsed operation of our device.

Importantly, the bandwidth and repetition rates available with the transducer demonstrated here are already sufficient to interface with leading microwave-frequency quantum systems, such as superconducting qubits. The electromechanical efficiency for short microwave pulses can be further improved by optimizing the design of the piezoelectric interface to restrict coupling to near-resonant modes. This change and switching of the microwave resonator from a transmission-based to a reflection-based coupling would increase the electromechanical efficiency by a factor of four. Additionally, the noise contributions can be reduced with improved optical resonator linewidth, which is readily achievable through the fabrication optimization of the lithium niobate block formation; typical silicon-on-insulator optomechanical photonic crystal cavities have demonstrated intrinsic optical linewidths as low as 200 MHz (refs. 34,39). When these improvements are combined, our transducer enters the regime where $N_{\text{add}} \ll 1$ and creating entanglement between remote qubits will be feasible³¹.

Conclusions

We have realized a scalable platform for microwave-to-optics transduction, based on an integrated mechanical mode that serves as an intermediary between the two electromagnetic fields. Constructing the device from thin-film lithium niobate on silicon allows us to realize efficient, low-noise and large-bandwidth transduction, through scalable fabrication techniques. We measure transduction efficiencies of 0.9% in the continuous and 5×10^{-5} in the pulsed regime while adding only around six photons of input-referred noise.

The fully integrated device with a surface area of less than 0.15 mm² only requires 1 nW of average laser power, allowing for repetition rates of up to 100 kHz. In terms of area and power dissipation, the current transducer design, therefore, directly allows for scaling to more than 10,000 transducers in a single dilution refrigerator. With optical-frequency multiplexing, these transducers could be used to interface a large-scale quantum processor using only around 100 fibres (with a predicted passive heatload of 300 pW (ref. 40)). Our device is also impedance matched to a 50 Ω line, allowing flexible connections to qubits located within the same dilution refrigerator. This enables complete separation between transduction and the qubit chip.

Our system is ideally suited to operate in the few-photon regime and optically read the state of a superconducting qubit, as has been recently demonstrated in another system⁴¹. The continuous transduction we achieve with nearly 1% efficiency combined with our large bandwidth should allow us to achieve a quantum readout efficiency of around 10^{-3} for pulses of several microseconds, enabling higher-fidelity readout. Here the requirements on added noise and efficiency are relaxed and our current performance is sufficient to achieve single-shot readout via the readout resonator of a qubit. Combined with optical multiplexing, this could lead to a system that replaces superconducting microwave amplifiers and cables, removing substantial heatload

and space restrictions inside a dilution refrigerator, enabling quantum processors to scale.

Online content

Any methods, additional references, Nature Portfolio reporting summaries, source data, extended data, supplementary information, acknowledgements, peer review information; details of author contributions and competing interests; and statements of data and code availability are available at <https://doi.org/10.1038/s41565-023-01515-y>.

References

- Kimble, H. J. The quantum internet. *Nature* **453**, 1023 (2008).
- Wehner, S., Elkouss, D. & Hanson, R. Quantum internet: a vision for the road ahead. *Science* **362**, eaam9288 (2018).
- Alexeev, Y. et al. Quantum computer systems for scientific discovery. *PRX Quantum* **2**, 017001 (2021).
- Ladd, T. D. et al. Quantum computers. *Nature* **464**, 45 (2010).
- de Leon, N. P. et al. Materials challenges and opportunities for quantum computing hardware. *Science* **372**, eabb2823 (2021).
- Gambetta, J. IBM Research Blog <https://research.ibm.com/blog/next-wave-quantum-centric-supercomputing> (2022).
- Awschalom, D. et al. Development of quantum interconnects (QICs) for next-generation information technologies. *PRX Quantum* **2**, 017002 (2021).
- Krastanov, S. et al. Optically-heralded entanglement of superconducting systems in quantum networks. *Phys. Rev. Lett.* **127**, 040503 (2021).
- Bravyi, S., Dial, O., Gambetta, J. M., Gil, D. & Nazario, Z. The future of quantum computing with superconducting qubits. *J. Appl. Phys.* **132**, 160902 (2022).
- Magnard, P. et al. Microwave quantum link between superconducting circuits housed in spatially separated cryogenic systems. *Phys. Rev. Lett.* **125**, 260502 (2020).
- McKenna, T. P. et al. Cryogenic microwave-to-optical conversion using a triply resonant lithium-niobate-on-sapphire transducer. *Optica* **7**, 1737 (2020).
- Xu, Y. et al. Bidirectional interconversion of microwave and light with thin-film lithium niobate. *Nat. Commun.* **12**, 4453 (2021).
- Sahu, R. et al. Quantum-enabled operation of a microwave-optical interface. *Nat. Commun.* **13**, 1276 (2022).
- Vainsencher, A., Satzinger, K. J., Peairs, G. A. & Cleland, A. N. Bi-directional conversion between microwave and optical frequencies in a piezoelectric optomechanical device. *Appl. Phys. Lett.* **109**, 033107 (2016).
- Jiang, W. et al. Efficient bidirectional piezo-optomechanical transduction between microwave and optical frequency. *Nat. Commun.* **11**, 1166 (2020).
- Mirhosseini, M., Sipahigil, A., Kalaei, M. & Painter, O. Superconducting qubit to optical photon transduction. *Nature* **588**, 599 (2020).
- Stockill, R. et al. Ultra-low-noise microwave to optics conversion in gallium phosphide. *Nat. Commun.* **13**, 2496 (2022).
- Higginbotham, A. P. et al. Electro-optic correlations improve an efficient mechanical converter. *Nat. Phys.* **14**, 1038 (2018).
- Arnold, G. et al. Converting microwave and telecom photons with a silicon photonic nanomechanical interface. *Nat. Commun.* **11**, 4460 (2020).
- Han, J. et al. Coherent microwave-to-optical conversion via six-wave mixing in Rydberg atoms. *Phys. Rev. Lett.* **120**, 093201 (2018).
- Fernandez-Gonzalvo, X., Horvath, S. P., Chen, Y. H. & Longdell, J. J. Cavity-enhanced Raman heterodyne spectroscopy in $\text{Er}^{3+}:\text{Y}_2\text{SiO}_5$ for microwave to optical signal conversion. *Phys. Rev. A* **100**, 033807 (2019).

22. Bartholomew, J. G. et al. On-chip coherent microwave-to-optical transduction mediated by ytterbium in YVO₄. *Nat. Commun.* **11**, 3266 (2020).
23. Hisatomi, R. et al. Bidirectional conversion between microwave and light via ferromagnetic magnons. *Phys. Rev. B* **93**, 174427 (2016).
24. Lauk, N. et al. Perspectives on quantum transduction. *Quantum Sci. Technol.* **5**, 20501 (2020).
25. Han, X., Fu, W., Zou, C.-L., Jiang, L. & Tang, H. X. Microwave-optical quantum frequency conversion. *Optica* **8**, 1050 (2021).
26. Siddiqi, I. Engineering high-coherence superconducting qubits. *Nat. Rev. Mat.* **10**, 875 (2021).
27. Krinner, S. et al. Realizing repeated quantum error correction in a distance-three surface code. *Nature* **605**, 669 (2022).
28. Horsman, C., Fowler, A., Devitt, S. & van Meter, R. Surface code quantum computing by lattice surgery. *New J. Phys.* **14**, 123011 (2012).
29. Beals, R. et al. Efficient distributed quantum computing. *Proc. R. Soc. A* **469**, 20120686 (2013).
30. Krinner, S. et al. Engineering cryogenic setups for 100-qubit scale superconducting circuit systems. *EPJ Quantum Technol.* **6**, 2 (2019).
31. Zeuthen, E., Schliesser, A., Sørensen, A. S. & Taylor, J. M. Figures of merit for quantum transducers. *Quantum Sci. Technol.* **5**, 34009 (2020).
32. Brubaker, B. M. et al. Optomechanical ground-state cooling in a continuous and efficient electro-optic transducer. *Phys. Rev. X* **12**, 021062 (2022).
33. Jiang, W. et al. Optically heralded microwave photon addition. *Nat. Phys.* <https://doi.org/10.1038/s41567-023-02129-w> (2023).
34. Chan, J., Safavi-Naeini, A. H., Hill, J. T., Meenehan, S. & Painter, O. Optimized optomechanical crystal cavity with acoustic radiation shield. *Appl. Phys. Lett.* **101**, 081115 (2012).
35. Aspelmeyer, M., Kippenberg, T. J. & Marquardt, F. Cavity optomechanics. *Rev. Mod. Phys.* **86**, 1391 (2014).
36. Xu, M., Han, X., Fu, W., Zou, C.-L. & Tang, H. X. Frequency-tunable high-Q superconducting resonators via wireless control of nonlinear kinetic inductance. *Appl. Phys. Lett.* **114**, 192601 (2019).
37. Kuwictsova, I. E., Zaitsev, B. D., Joshi, S. G. & Borodina, I. A. Investigation of acoustic waves in thin plates of lithium niobate and lithium tantalate. *IEEE Trans. Ultrason., Ferroelectr., Freq. Control* **48**, 322 (2001).
38. Riedinger, R. et al. Non-classical correlations between single photons and phonons from a mechanical oscillator. *Nature* **530**, 313 (2016).
39. Qiu, L., Shomroni, I., Seidler, P. & Kippenberg, T. J. Laser cooling of a nanomechanical oscillator to its zero-point energy. *Phys. Rev. Lett.* **124**, 173601 (2020).
40. Lecocq, F. et al. Control and readout of a superconducting qubit using a photonic link. *Nature* **591**, 575 (2021).
41. Delaney, R. D. et al. Superconducting-qubit readout via low-backaction electro-optic transduction. *Nature* **606**, 489 (2022).

Publisher's note Springer Nature remains neutral with regard to jurisdictional claims in published maps and institutional affiliations.

Springer Nature or its licensor (e.g. a society or other partner) holds exclusive rights to this article under a publishing agreement with the author(s) or other rightsholder(s); author self-archiving of the accepted manuscript version of this article is solely governed by the terms of such publishing agreement and applicable law.

© The Author(s), under exclusive licence to Springer Nature Limited 2023

Data availability

Source data for the figures are available via Zenodo at <https://doi.org/10.5281/zenodo.8232627>.

Acknowledgements

We would like to thank A. Safavi-Naeini for valuable discussions and support. We thank J. van Oven and D. de Jong at Qblox for technical support. We further gratefully acknowledge assistance from E. He, helpful discussions with C. Jurczak and J. Fink, supply of wafers from NGK Insulators and the hospitality of the Department of Quantum Nanoscience at Delft University of Technology and the Kavli Nanolab Delft. This work is financially supported by the European Innovation Council (EIC Accelerator QModem 190109269) and the Province of Zuid-Holland (R&D samenwerkingsproject QConnect).

Author contributions

All authors contributed to the simulation, fabrication and testing of the device. P.D., S.S. and M.L. fabricated the device. M.J.W., A.C.B., R.S., B.H., T.C.v.T. and F.H. performed the experiments described in the manuscript. B.H., S.S. and R.S. simulated the device performance.

M.J.W., R.S., S.G., A.C.B. and B.H. wrote the manuscript with input and editing from all authors.

Competing interests

All authors are or have been employed by QphoX B.V. and are, have been, or may in the future be participants in incentive stock plans at QphoX B.V. The authors declare that they have no competing interests.

Additional information

Supplementary information The online version contains supplementary material available at <https://doi.org/10.1038/s41565-023-01515-y>.

Correspondence and requests for materials should be addressed to Simon Gröblacher or Robert Stockill.

Peer review information *Nature Nanotechnology* thanks the anonymous reviewers for their contribution to the peer review of this work.

Reprints and permissions information is available at www.nature.com/reprints.